Photoluminescent Response in Carbon Nanomaterials to Enzymatic Degradation

*Xiaoyun He,[†] David L. White,[†] Alexandr A. Kapralov,[‡] Valerian E. Kagan,[†‡] Alexander Star[†§]**

[†]Department of Chemistry, University of Pittsburgh, Pittsburgh, Pennsylvania 15260, USA

[‡]Department of Environmental and Occupational Health, University of Pittsburgh, Pittsburgh, Pennsylvania 15261, USA

[§]Department of Bioengineering, University of Pittsburgh, Pittsburgh, Pennsylvania 15261, USA

Keywords: carbon nanotubes, graphene oxide, fluorescence, myeloperoxidase, sensors

Abstract

Myeloperoxidase (MPO), a key enzyme released by neutrophils during inflammation, has been shown to catalyze the biodegradation of carbon nanomaterials. In this work, we perform photoluminescence studies on the MPO-catalyzed oxidation of graphene oxide (GO) and surfactant-coated pristine (6,5) single-walled carbon nanotubes (SWCNTs). The enzymatic degradation mechanism involves the introduction of defects, which promote further degradation. Interestingly, the photoluminescent responses of GO and SWCNTs to enzymatic

degradation are counterposed. While near infrared (NIR) fluorescence intensity of SWCNTs at 998 nm is either unchanged or decreases dependent on the surfactant identity; blue fluorescence intensity of GO at 440 nm increases with the progression of oxidation by MPO/H_2O_2/Cl^- due to the formation of graphene quantum dots (GQDs). Turn-on GO fluorescence is also observed with neutrophil-like HL-60 cells, indicative of potential applications of GO for imaging MPO activity in live cells. Based on these results, we further construct two ratiometric sensors using SWCNT/GO nanoscrolls by incorporating surfactant-wrapped pristine SWCNTs as the internal either turn-off (with sodium cholate (SC)) or reference (with carboxymethycellulose (CMC)) sensor. The ratiometric approach enables the sensors to be more stable to external noise by providing response invariant to the absolute intensity emitted from the sensors. Our sensors show linear response to MPO oxidative machinery, and hold the promise to be used as self-calibrating carbon nanomaterial-based MPO activity indicators.

Introduction

Myeloperoxidase (MPO) is a crucial peroxidase secreted by various primary phagocytic cells of the innate immune system.[1] In particular, MPO is most abundantly expressed by neutrophils during the first phase of inflammation. MPO produces potent oxidants such as hypochlorous acid (HOCl) and other reactive intermediates which are essential to destroy pathogens.[2-4] MPO enzymatic oxidative degradation of carbon nanomaterials has been previously demonstrated both *in vitro* and *in vivo*.[5, 6] Specifically, Kagan *et al*.[3] reported that, on incubation with MPO, H_2O_2, and Cl^-, carboxylated single-walled carbon nanotubes (SWCNTs) can be degraded into a series of carbonaceous by-products including but not limited to CO, CO_2, and a range of hydrocarbons. The enzymatic oxidation of gold nanoparticle-corked nitrogen-doped carbon nanotube cups (NCNCs) was also recently proposed as a drug delivery mechanism.[7] The enhanced enzymatic oxidation activity in tumor microenvironment was utilized as a trigger to open the gold-corked NCNCs, representing a novel cancer immunotherapy approach using NCNCs as effective drug nanocarriers for the delivery of

paclitaxel.[8] In addition to carbon nanotubes, Kurapati *et al*.[9] has reported the biodegradation of graphene oxide (GO) sheets by MPO in the presence of 200 μM H_2O_2. *In vitro* oxidation of GO by neutrophils and generated degradation products have also been demonstrated to be non-genotoxic.[10]

While there have been numerous studies[11] of biodegradation of carbon-based nanomaterials, the utilization of fluorescence spectroscopy to characterize carbon nanomaterials and monitor their chemical changes during enzymatic oxidation has not been investigated. The photoluminescence (PL) properties of carbon nanomaterials are closely related to their size, morphology, and the existence of defect sites.[12, 13] PL spectroscopy provides opportunities to both elucidate the mechanism of biodegradation as well as an analytical tool to measure the underlying MPO activity. We had previously concluded that MPO/H_2O_2/Cl^- enzymatic degradation was a relatively complete oxidation process for oxidized HiPco SWCNTs based on PL measurements. This is in contrast to the milder oxidation catalyzed by a plant-based enzyme horseradish peroxidase (HRP).[14] We also investigated the role of different surfactants in the MPO-catalyzed degradation of pristine SWCNTs.[15] The band gap emissions of sodium cholate-, DNA-, and albumin-coated nanotubes (SC/DNA/BSA-SWCNTs) were quenched in a diameter-dependent fashion.

Commercial probes for detecting MPO activity measure reactive oxygen species (ROS), important antimicrobial agents generated by MPO during the immune response.[16] Such sensors have been validated by electron paramagnetic resonance spectroscopy, photoluminescence spectroscopy, magnetic resonance imaging,[17-19] and electrochemical methods.[20-22] Carbon nanodots,[23-25] SWCNTs,[26, 27] GO,[28] and reduced GO (rGO),[29, 30] have recently been explored as sensor candidates for the detection of MPO activity in both *in vitro* and *in vivo* environments. The complexity of MPO/H_2O_2/Cl^- oxidative machinery makes targeting one or several MPO-generated oxidants less representative of the overall MPO activity. Most of the current generation of carbon nanomaterials-based fluorescent sensors were based on single fluorophore. In comparison, ratiometric sensors utilize two different fluorescent signals as internal

references for each other. Ratiometric sensors provide a built-in correction for environmental interference, improve the signal-to-noise ratio, and broaden the linear range.[31]

In this work, to address the above concerns, we systematically investigated the enzymatic degradation mechanism of SWCNTs and GO via photoluminescence. Based on our findings of the PL progression during MPO/H_2O_2/Cl^- oxidation, we constructed two ratiometric fluorescent sensors as sacrificial MPO indicators for *in vitro* environments.

Materials and Methods

Cobalt-molybdenum-catalyzed (CoMoCAT) single-walled (6,5) carbon nanotubes were purchased from Sigma-Aldrich and used without further purification. Aqueous SWCNT suspensions were initially prepared at 1 mg/mL with either 1 wt% sodium cholate (SC, Sigma-Aldrich) or 0.5 wt% sodium carboxymethylcellulose (CMC, Sigma-Aldrich) as a surfactant. The suspensions were sonicated for 1 h and centrifuged to remove large SWCNT bundles. The top 90% of the supernatant was transferred to a separate container and used as a stock solution. GO aqueous solution (5 mg/mL) was purchased from Graphene Supermarket. SWCNT/GO nanoscrolls were synthesized by sonicating a mixture of 0.5 mg/mL surfactant-coated SWCNTs and 1 mg/mL GO for 1 h.

For MPO enzymatic degradation experiments, six vials were prepared by adding 446 µL 1× phosphate buffer saline (PBS) (Sigma-Aldrich, 0.01 M phosphate buffer, 0.0027 M potassium chloride and 0.137 M sodium chloride, pH 7.4, at 25°C) and 50 µL of each sample (1 mg/mL GO, 0.5 mg/mL SWCNT, and GO/SWCNT). Lyophilized MPO (Athens Research & Technology, Inc.) was dissolved in 1× PBS with a final concentration of 2.5 µg/µL and added to all six vials at a volume of 2 µL. The MPO/H_2O_2/Cl^- degradation was activated by adding 2 µL 25 mM H_2O_2 (Fisher Scientific) every hour with total seven additions per day for 5 days. 2 µL MPO were replenished daily to compensate for the loss. For control experiments without (i) carbon nanomaterials, (ii) MPO, (iii) H_2O_2, and (iv) Cl^-, equal volumes of (i) nanopure H_2O, (ii) PBS, (iii) nanopure H_2O, and (iv) 1×phosphate buffer solution were added to the

degradation system at indicated time-points as a substitute for (i) carbon nanomaterials, (ii) MPO, (iii) H_2O_2, and (iv) PBS, respectively.

For cellular degradation of GO, human myeloid leukemia HL-60 cells were chosen and induced to differentiate into neutrophil-like cells by addition of 1.5% dimethyl sulfoxide (DMSO) for 6 days. Differentiated cells were suspended in RPMI 1640 media without phenol red and seeded in 6-well plates with a volume of 2 ml in each well. GO was added in concentration of 0.035 mg/mL and incubated in the presence of N-formyl-methionyl-leucyl-phenylalanine (fMLP, 100 nM) and cytochalasin B (CyB, 5 µg/mL). After 24-h incubation, samples were centrifuged at 700 × g for 5 min and the supernatant was taken for fluorescence and TEM measurements. The 0 h control sample, GO (0h), was prepared by dissolving GO in RPMI 1640 media (without phenol red) at a concentration of 0.035 mg/mL, centrifugated immediately after dissolving. For experiments without GO, cells incubated with fMLP and CyB were centrifuged down at either 0 h or 24 h, respectively, and the supernatant was collected for fluorescence measurements.

UV-vis-NIR absorption spectra were collected using PerkinElmer Lambda 900 spectrophotometer over the wavelength range of 200 − 1200 nm. Raman spectra were acquired on XploRA plus confocal Raman microscope (Horiba) with 638 nm laser (24mW) operating at 10% power.

Visible photoluminescence spectra were obtained using a Fluoromax-3 spectrometer (HORIBA Jobin Yvon) equipped with a xenon lamp light source and a photomultiplier tube detector. All visible emission spectra were recorded with 325 nm excitation unless otherwise stated. Slit width were set at 10 nm and 3 nm for measurements of all MPO/H_2O_2/Cl^- and HL-60 cell degradation experiments, respectively.

NIR photoluminescence measurements were performed on a Nanolog spectrofluorometer (HORIBA Jobin Yvon) equipped with a xenon lamp (400 W) light source, double excitation monochromators, and Symphony II InGaAs array (NIR) detector. Spectra were obtained using 566 nm excitation wavelength, which is in resonance with the first absorption band of the (6,5) SWCNTs. Slit widths were set at 10 nm for both excitation and

emission. All measurements were obtained with an 830 nm long-pass filter at ambient temperature.

Transmission Electron Microscopy (TEM, FEI Morgagni, 80 keV) samples were prepared by dropcasting 6 µL of 100x diluted solution on a lacey carbon grid and dried in ambient conditions overnight.

The hydrodynamic diameter (by dynamic light scattering (DLS)) and zeta-potential of samples in nanopore water were obtained using Zetasizer Nano ZS90 (Malvern Panalytical Ltd). DLS were carried out with 1 mL samples under 633 nm laser irradiation. Each measurement was performed in triplicate. The zeta-potential measurements were conducted in the phase analysis light scattering (PALS) mode following the solution equilibration at 25°C. Each sample was measured three times and the average data was taken.

Atomic Force Microscopy (AFM) was taken using Bruker multimode 8 utilizing a Veeco Nanoscope IIIa controller in tapping mode. An AppNano ACST-SS probes having nominal radius of 1−2 nm was operated at a frequency of 160−225 kHz, an amplitude set point of 1.70−1.75 V, and a drive amplitude of 100−300 mV. Samples were made by dropcasting 10 µl of 10 times diluted respective nanoscroll solution onto freshly cleaved mica and left to dry under vacuum for at least two hours. SWCNT(CMC)/GO nanoscrolls were additionally subjected to a 24-hour dialysis procedure using a 90 kDa filter before dropcasting to make identification of one-dimensional structures easier. All images were processed in Gwyiddon.

Results and Discussion

Mechanisms of the MPO enzymatic oxidative machinery, peroxidase cycle and halogenation cycle, are summarized in Figure 1a. MPO is a heme-containing protein with Fe(III)-protoporphyrin IX as its active site. Initially, MPO is inactive and its heme group is in the ferric resting state. The interaction with hydrogen peroxide (H_2O_2) induces the active center to produce the oxidative ferryl oxo iron (Fe^{4+}=O), and porphyrin (Por) π radical cation, collectively known as compound I, through a protein-assisted conversion. The generated

oxidant can return to the resting state via two pathways. It can be reduced directly to the resting state by the conversion of Cl^- to hypochlorous acid in the acidic environment of neutrophils (red path). Otherwise, the reduction happens in two sequential one-electron transfer steps. Compound I is reduced to Compound II and then to the resting state, as the substrates (GO, SWCNTs, and/or SWCNT/GO nanoscrolls) are oxidized accordingly and form radical oxidative products.

The defect sites of carbon nanomaterials, such as pre-existing oxygen-containing functional groups in GO or hypochlorite (ClO^-) generated oxidative defects on the surface of SWCNTs,[32, 33] serve as the initiation centers of MPO-catalyzed biodegradation.[34, 35] The interaction between defect sites of carbon nanomaterials and strong oxidants, ClO^- and Compound I, facilitate the degradation of the material's structure. As shown in Figure 1b, oxidative damage of SWCNTs results in shortened tubes with a variety of oxygen-containing defects, such as hydroxyl, ether, epoxide, and carboxyl groups on the surface. In contrast, holes gradually appear in the GO sheets resulting in the formation of graphene quantum dots (GQDs).[9, 36] The ultimate shape and size of resulting GQDs is dictated by the pre-existing pristine sp^2 domains in GO sheets. While GO transitions from two-dimensional to zero dimensional morphology,[9, 36] SWCNTs retain their characteristic one-dimensional nanotube structure after $MPO/H_2O_2/Cl^-$ treatment.[3] The less effective degradation can be attributed to the lack of the pre-existed oxygen-containing defect sites in pristine SWCNTs with respect to GO.[3]

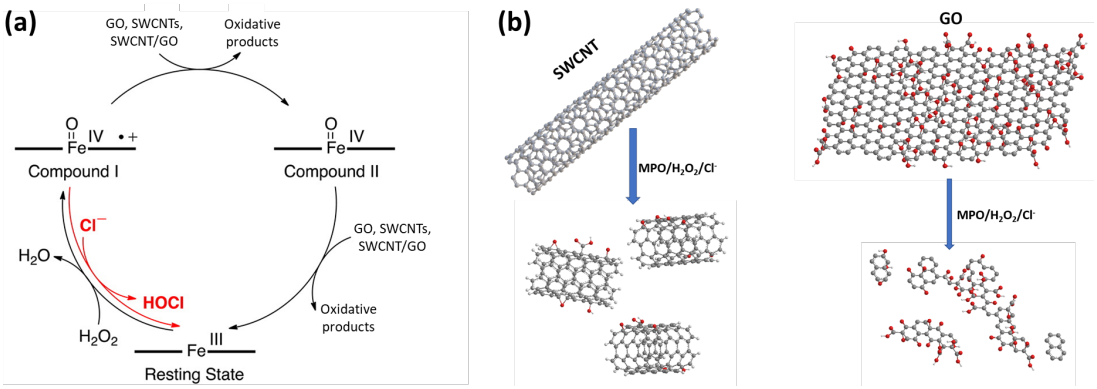

Figure 1. (a) The catalytic peroxidase and halogenation cycles of MPO. Adapted with permission from ref. 35. Copyright 2012 American Chemical Society. (b) A schematic

diagram illustrating the enzymatic degradation of SWCNTs and GO. (Carbon and oxygen atoms are shown in gray and red, respectively).

Our previous results indicate that using sodium cholate (SC) as a surfactant, the NIR fluorescence of pristine SWCNTs is suppressed following the introduction of defects on the sidewalls of SWCNTs.[14, 15] As shown in Figure S1, SC wrapped SWCNTs displayed a gradual decrease in both absorbance and PL intensity over the 5-day MPO/H_2O_2/Cl^- degradation. In this study, we tested another surfactant, carboxymethylcellulose (CMC), because of its favorable biocompatibility[37, 38] and the potential as an ideal matrix of thin-film sensors.[39, 40] Figure 2a displays the UV-vis-NIR spectra of CMC-coated SWCNTs over the 5-day oxidation. Although there was a small gradual decrease in absorbance of Day 5 sample, the day 5 spectrum retained the three absorption peaks centered at around 1000 nm, 575 nm, and 345 nm corresponding to the characteristic E_{11}, E_{22}, and E_{33} excitonic transitions of (6,5)-SWCNTs.[41] The small decrease in absorbance can be a result of the reaction mixture dilution by continuously replenishing H_2O_2 and MPO over 5-day degradation process (Figure S2), the slight degradation of SWCNTs in response to MPO oxidative machinery, and experimental variations. However, in contrast to SC (Figure S1a), the retained absorption behavior of CMC wrapped SWCNTs indicates the inhibition of previously observed MPO degradation of SWCNTs using other surfactants.[14, 15] The progressive PL intensity of CMC-wrapped SWCNTs in Figure 2b showed slight decreases in the process of 5-day oxidative degradation, while remaining the characteristic E_{11} emission peak of SWCNTs in day 5 sample . Excitation-emission (EE) maps in Figure S3 further confirmed the retained characteristic E_{11} emission peak after 5-day degradation with little peak shift. The consistency of PL intensity is indicative of the lack of defect sites formed on the surface of the exposed bare SWCNTs after the CMC wrapping. The observed surfactant-dependent reactivity[42] implies that, compared with SC, CMC protects the surface of SWCNTs through a higher surface coverage. With less bare SWCNTs surface exposed to the strong oxidants generated in the MPO peroxidase and halogenation cycles (Figure 1a), fewer oxygen-

containing defects will be generated. As those defects serve as the initiation centers of degradation,[34, 35] fewer generated defect sites will make CMC-wrapped SWCNTs less susceptible to the MPO oxidative machinery, and thus exhibited the diminished reactivity as compared to SWCNT(SC). The PL consistency of SWCNT(CMC) over 5-day degradation was demonstrated by triplicate measurements (Figure S4), indicating its potential as being a reference sensor for MPO oxidative machinery.

In order to further confirm the factors affecting the change of PL intensity, three control experiments were performed without addition of MPO, H_2O_2, and Cl^-, respectively. As shown in Figure S5a, similar to complete degradation systems, characteristic E_{11}, E_{22}, and E_{33} excitonic transitions of (6,5)-SWCNTs remained in all three samples after 5-day degradation, Consistently, the PL intensity (Figure S5b) of three controls after 5-day oxidation displayed comparable intensity to that under complete MPO/H_2O_2/Cl^- degradation systems. This result revealed that the slight decrease in PL intensity in Figure 2b is a combined effect of the solution dilution, experimental variance, and modest SWCNTs oxidation. The fluorescence background in the absence of SWCNTs was also being tested to exclude its contribution to the observed PL. As shown in Figure S6, the background PL at SWCNTs E_{11} emission across 5-day oxidation is negligible and the change in the intensity is minimal compared to samples with SWCNTs (Figure 2b).

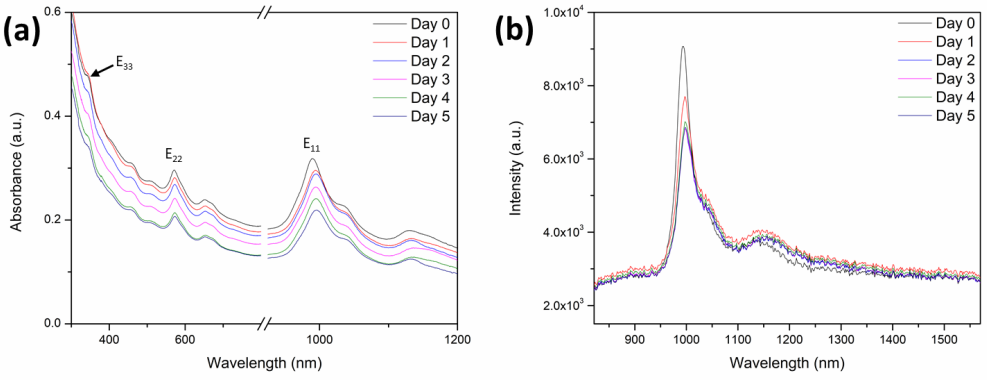

Figure 2. UV-vis-NIR absorption spectra (a) and photoluminescence emission spectra (b) of MPO/H_2O_2/Cl^- degradation of SWCNT (CMC wrapped) from Day 0 to Day 5.

The progressive spectra of GO substrates were also measured. Prior to the oxidation, the UV-vis-NIR absorption spectrum of pristine GO (Figure 3a) displayed one peak centered at 230 nm related to the π-π* transition of the aromatic C-C bond, and another shoulder peak at around 300 nm corresponding to the n-π* of the C=O bond transition. These two prominent features were gradually attenuated as a result of the 5-day oxidation treatment, demonstrating the degradation of the chemical structure of GO. Consistent with previous studies,[9, 10, 43] the characteristic D (~ 1320 cm^{-1}) and G (~ 1570 cm^{-1}) bands of GO in the Raman spectra (Figure 3b) disappeared after a 5-day MPO/H_2O_2/Cl^- degradation. Transmission electron microscopy (TEM) reveals structural changes in GO before and after the 5-day MPO/H_2O_2/Cl^- oxidation (Figure 3c and 3d). In contrast to the micrometer-sized GO single-layer sheet initially present, small GQDs with a diameter around 20 nm (Figure S7) were observed after 5 days of oxidation.

The progression of MPO catalyzed oxidation of GO over 5 days was monitored using fluorescence spectroscopy. Interestingly, a broad emission peak centered at 440 nm (Figure 3e, Figure S8b), with an excitation peak centered at 325 nm (Figure 3f), gradually appeared over the 5-day degradation. Similar blue-luminescent GQDs have been previously observed during a photo-Fenton oxidation reaction of GO[36, 44] while having never been reported in the context of biodegradation system.[11] The peak evolution had monotonic increases under different excitation wavelengths ranging from 275 to 375 nm over the time course (Figure S9). The oxidation-generated photoluminescence exhibited an excitation wavelength dependence (Figure S10). The emission peak position was located at 440 nm under the 300 nm excitation, and red-shifted 10-20 nm under either higher (275 nm) or lower excitation energy (350 and 375 nm). The highest intensity PL emission was observed under the 325 nm excitation, approximately 1.5 times higher than the second most intense peak under the 350 nm excitation. The PL emission spectra of GO features a minor peak at 367 nm that can be assigned as the water Raman peak. Water Raman peaks were also observed across different excitation wavelengths (Figure S10), their positions agreed well with calculated values (Table S1). Since the focus of this work is the PL evolution due to the GO degradation producs, the solvent Raman peak intensity should be minimal. Under different excitations, GQDs PL peaks are all well-

resolved from the water Raman peaks (Figure 3e and S10). Thus, the interference and possible distortion of the fluorescence spectra due to the solvent Raman peak is negligible. Since the 325 nm excitation gave rise to the highest relative intensity of the degradation products' PL peak (at 440 nm) to the water Raman peak, it was selected for the further use in MPO-secreting cells degradation experiments and the dual-emission ratiometric sensors due to the brightness of the emission as compared to matrix effects. Furthermore, the standard deviation of the normalized PL intensity was as low as 0.12 for three replicate mesurements (Figure S11), which indicates the favorable reproducibility of the GO substrate being a turn-on sensor for MPO oxidative machinery.

In order to confirm the necessity of the complete MPO/H_2O_2/Cl^- oxidation system for the degradation of GO, three control experiments were performed by removing MPO, H_2O_2, and Cl^-, respectively. As compared to the complete disappearance of characteristic GO peaks in the complete oxidation system, the UV-vis-NIR spectra of all three control samples (Figure S12a) still exhibited strong absorbance in the UV range (200-300 nm) with a minor degree of attenuation. The integrity of GO was observed via Raman spectroscopy of the characteristic D and G bands of GO were still present in all three controls after the 5-day oxidation (Figure S12b). The Raman and UV-vis-NIR absorption results both indicate that the biodegradation of GO was markedly suppressed in all of three controls. Further evidence was collected by TEM (Figure S13) as intact single-layer GO sheets were still present in all three 5-day degradation samples. The PL spectra of all three controls displayed negligible increases of the PL emission centered at 440 nm (Figure S14a) and excitation centered at 325 nm (Figure S14b). These results are consistent with previous studies where carbon nanotubes were shown to undergo incomplete MPO catalyzed degradation in the absence of chloride.[3] Missing one or more components in the peroxidase and halogenation cycles (Figure 1a) weakens the overall oxidation potential resulting in the less efficient degradation of GO.

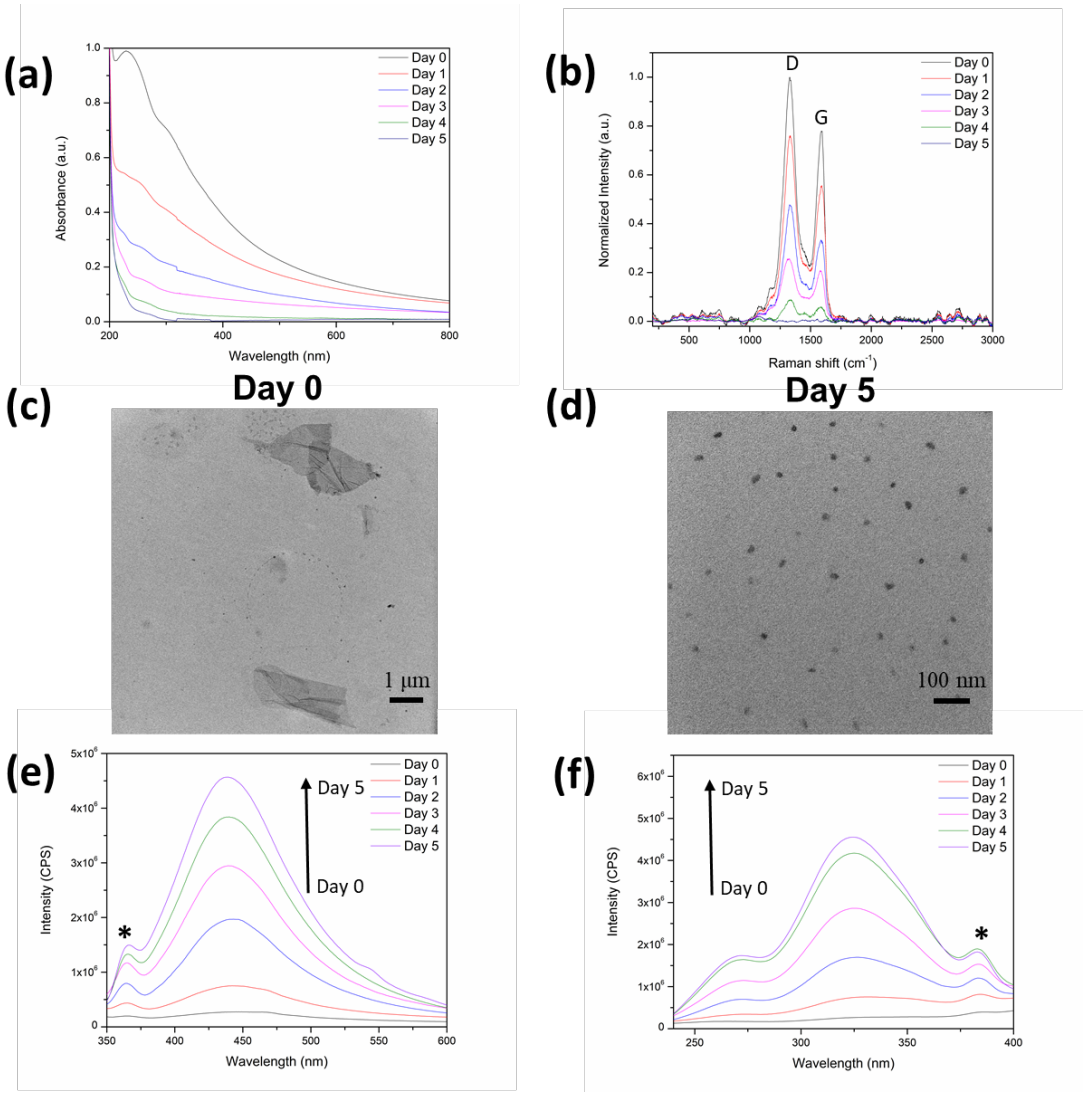

Figure 3. UV-vis-NIR spectra (a), Raman spectra (b), TEM images (c, d), photoluminescence emission (e) and excitation (f) spectra of the 5-day MPO/H_2O_2/Cl^- degradation of GO. (*) is water Raman peak. The PL emission spectra (e) were obtained with excitation at 325 nm. The excitation spectra (f) were obtained at emission wavelength 440 nm.

To exclude the possibility that the background fluorescence was the primary contributor to increased PL, a control experiment was performed in the absence of GO. As shown in Figure S15a and S15b, different from the GO-based observations (Figure 3e and 3f), one emission peak centered at 400 nm was observed with an excitation peak at 290 nm, attributed to the formation of fluorescent compound dityrosine.[45, 46] Further background subtraction was performed on the PL spectrum of 5-day GO degradation sample. As shown in

Figure S16, one peak centered at around 445 nm remained after the background subtraction, and was assigned to the formation of GO degradation products.

PL studies of SWCNTs degradation by neutrophils have been previously reported by our group.[15] A more efficient PL quenching was observed when incubating with neutrophils as compared to MPO alone. Previous studies also indicate neutrophils' ability to extracellularly degrade GO *in vitro* through an MPO-catalyzed mechanism by Raman spectroscopy.[10] Thus, in this work, we proceeded to apply the fluorescence spectroscopy to study the degradation of GO by MPO-secreting cells. Figure 4a and 4b show the fluorescence emission spectra under different excitation wavelengths. The RPMI 1640 media (dashed lines) displayed a strong background fluorescence centered at 410 nm and 350 nm which is attributed to the combined effect of autofluorescence components like tryptophan[47] and folic acid.[48] As the media itself contains L-tyrosine which is convertible into dityrosine, an intensely fluorescent compound, under the oxidative environment, the small decrease of the background fluorescence (Figure 4a and 4b, dashed black line vs. dashed red line) under both excitations indicates that the formation of dityrosine is actually negligible in our experimental condition without the existence of GO. The main contributor of the background fluorescence remains to be its autofluorescence without the presence of GO. Although the media did increase background fluorescence, samples with GO after 24-h incubation (solid red lines) displayed an increase of fluorescence emission with respect to corresponding 0-h samples (solid black lines) as well as higher intensity than 24-h background (dashed red lines). Interestingly, under 300 nm excitation, one broad emission peak at 400-450 nm was formed exclusively with sample containing GO after incubating with cells after 24 hours (Figure 4b, red line). This additional shoulder peak is not observed under 325 nm excitation and unique with respect to all other samples under 300 nm excitation, thus could be served as a direct clue indicating the possible formation of GO degradation products. Distinguishable fluorescent features stem from the GO oxidative products as evidenced by the dark dots in TEM images (Figure 4c). The background subtraction of PL emission in both excitations conditions reveals a peak centered at around 410 nm (Figure 4a and 4b insets), similar to the spectra of dityrosine.[45, 46] We reasoned that, while the dityrosine formation is

negligible in the absence of GO, the conversion could be increased with the existence of GO. It has been reported[49] that carbon nanomaterials could elicit specific immune response pathway. The increased generation of oxidants will thus lead to more dityrosine formation. Secondly, compared with the direct addition of MPO in the MPO/H_2O_2/Cl^- oxidation, the existence of micrometer-sized cells[50] could interfere with the interaction between the secreted MPO and GO, and lead to the higher production of the byproducts, dityrosine. Consequently, the strong fluorescence of dityrosine may mask the fluorescence of GO degradation products. Although this result is limited to the detection of GO oxidative products over dityrosine background in terms of PL, it shows that fluorescence spectroscopy can be applied as an analytical tool to study GO biodegradation by giving distinguishable PL response between sample containing GO degradation products with other control samples based on either peak intensity or peak position. As for the further improvement of the detectability of GO degradation products vs. dityrosine, time-resolved photoluminescence technique could be a good candidate with regard to the possible different decay profiles of these two species,[51-54] while it is beyond the scope of this work.

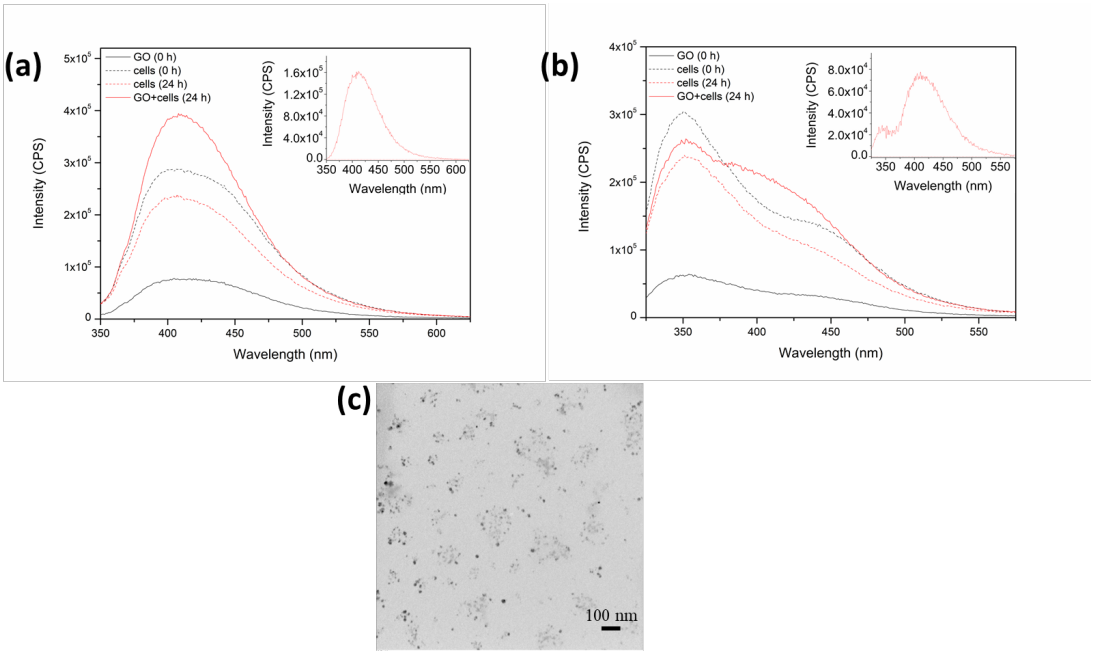

Figure 4. Fluorescence emission spectra of the degradation of GO with neutrophil-like HL-60 cells under 325 nm (a) and 300 nm (b) excitation. (Cells were centrifuged down before taking

the measurements). The insets show the PL spectra of samples containing GO after the 24-h incubation with cells after background subtraction (samples containing cells only after 24-h incubation (dashed red lines) were served as the background, as they shown a flat line in the insets). TEM image (c) of the supernatant of sample containing GO after the 24-h incubation with cells.

In the interest of developing sensors which can be calibrated in complex backgrounds, we combined the insights regarding GO and SWCNTs in the presence of MPO degradation to develop two dual emission ratiometric sensors with SC-coated or CMC-coated SWCNTs wrapped in GO (nanoscrolls). Although there is minimal PL background in the NIR range (Figure S6), the ratiometric strategy, as shown previously,[55-57] could overcome the limitations of the relative strong visible PL background (Figure S15 and S16). Using the ratio of PL intensity of two fluorophores, the background optical interference is being effectively eliminated. The GO-wrapped SWCNTs nanoscrolls were synthesized according to the published sonication procedure.[58] The spontaneous formation of the core-shell structure is a result of the strong hydrogen bonding between the hydrophilic surface of both GO[59, 60] and surfactant-coated SWCNTs. Additionally, the strong π-π stacking non-covalent interaction between the GO and the exposed bare CNTs surface provides another driving force for wrapping.[58-61] Zeta-potential values of these two types of nanoscrolls (Figure 5a) are representative of the magnitude of electrostatic interactions between colloidal particles and indicative of their colloidal stability. Both systems exhibited relatively large zeta-potentials (–34.8 ± 13.9 and –41.5 ± 9.0 mV for SWCNT(SC)/GO and SWCNT(CMC)/GO, respectively), suggestive of the long-term suspendability from the electrostatic considerations. However, both hybrids exhibited lower zeta-potentials than the corresponding SWCNT precursors (–39.8 ± 8.62 and –53.2 ± 7.47 mV for SWCNT(SC) and SWCNT(CMC), respectively), highlighting differential charge density present in the surfactant-wrapped SWCNTs[62] as opposed to the complete composites. It should be noted that DLS measures the hydrodynamic radii of spherical

particles, thus the absolute values (Figure 5a) may not reflect the actual sizes of GO, SWCNTs, and SWCNT/GO. However, complementary to location-specific TEM characterization, DLS data confirms the relatively narrow size distribution across each sample as they were acquired by analyzing the bulk sample as a whole. More importantly, the relative 60-100 nm increases and significant decreases of both nanoscrolls (222 ± 78 and 349 ± 182 nm for SWCNT(SC)/GO and SWCNT(CMC)/GO, respectively) with respect to their corresponding SWCNTs precursors (120 ± 84 and 285 ± 111 nm for SWCNT(SC) and SWCNT(CMC), respectively) and GO (2400 ± 691 nm) precursors, respectively, further support the success SWCNTs wrapping and the conformational change of GO. This conclusion is in consistent with both previously published work[63] and the TEM results (Figure 5b and 5c). Figure 5b and 5c show the TEM images of synthesized nanoscrolls, revealing that GO sheets were successfully wrapped around the nanotubes. AFM images and line profiles of both nanoscrolls are shown in Figure S17. The SC- and CMC-wrapped nanotubes displayed the diameters of approximately 0.8 – 1.4 nm (Figure S17a) and 2 – 4 nm (Figure S17b), respectively, in accordance with previous work.[64, 65] The line profiles also showed a maximum ~ 2.5 nm (Figure S17a, Trace 2) and ~ 12 nm (Figure S17b, Trace 1) in diameter of SWCNT(SC) and SWCNT(CMC), respectively, which are greater than that of the correspondingly surfactant-wrapped nanotubes. This observation further demonstrated the successful formation of nanoscrolls through the wrapping of GO on the surface of SWCNTs.

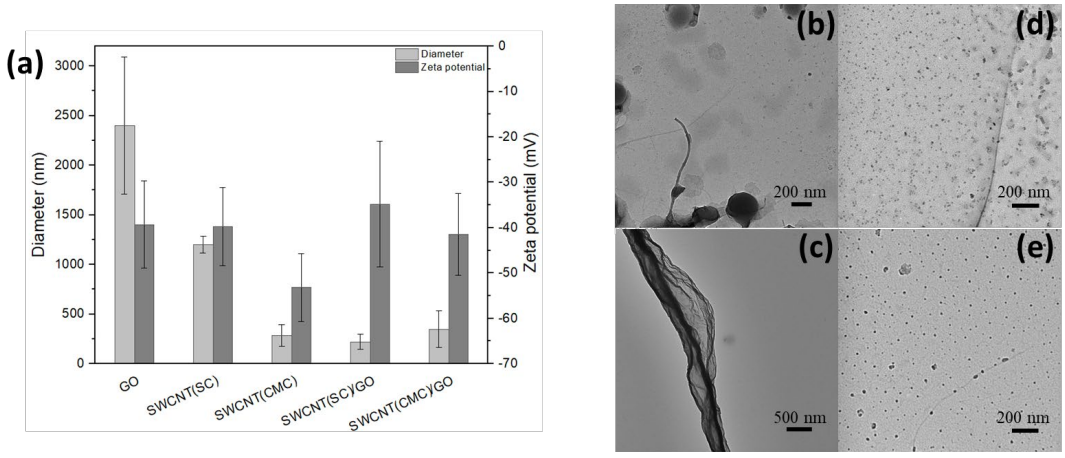

Figure 5. (a) Diameter (by DLS) and zeta potential of different samples. TEM images of SWCNT(SC)/GO (b, d) or SWCNT(CMC)/GO (c, e) before (b, c) and after (d, e) the 5-day MPO/H_2O_2/Cl^- degradation.

After degradation, TEM images illustrate that GO was preferentially degraded resulting in the formation of GQDs, while SWCNTs were still observable in both 5-day oxidation samples (Figure 5d and 5e). Figure S18 shows the UV-vis-NIR spectra of the two nanoscrolls systems during the MPO-mediated degradation. Before oxidation, both nanoscrolls displayed characteristic absorption peaks of both GO (around 230 nm) and SWCNTs (~990 nm for the first (E_{11}) and ~570 nm for the second (E_{22}) excitonic transitions), which indicates the successful construction of both nanoscrolls. Analogous to the individual oxidation of GO (Figure 3a), after the 5-day degradation, the characteristic GO peaks disappeared completely in both nanoscrolls systems, demonstrating the complete degradation of GO. After 5 days of the MPO-driven degradation, the characteristic absorption and NIR fluorescent peaks of SWCNTs remained for both samples (Figure S18 and Figure 6), consistent with the TEM results (Figure 5d and 5e). SWCNT(CMC)/GO composites showed less degradation than the SWCNT(SC)/GO composites. This determination was made by the degree of decrease from Day 0 to Day 5 in both UV-vis-NIR (Figure S18) and NIR fluorescence spectra (Figure 6). The surfactant-dependent oxidation was also consistent with the individual CMC-SWCNTs (Figure 2) or SC-SWCNTs[15] (Figure S1) subjected to enzymatic degradation.

Figure 6 shows the change in the fluorescence intensity of two types of SWCNT/GO nanoscrolls during the 5-day enzymatic oxidation. Increasing fluorescence emission centered at 420 nm for SWCNT(SC)/GO and 430 nm and SWCNT(CMC)/GO was observed. We attributed this emission to the oxidation of wrapped GO sheets on the outer side of the nanoscrolls core/shell structures (Figure 6c). This result was in accordance with the degradation occurring on the GO sheets individually (Figure 3e). The blue shifted emission can be accounted for by solvatochromism,[66, 67] induced by incorporating surfactant-coated SWCNTs. The SWCNTs NIR bandgap emission slowly decreased for SWCNT(SC)/GO

nanoscrolls (Figure 6a) upon the generation of defect sites on the surface of SWCNTs (Figure 6c). SWCNT(CMC)/GO nanoscrolls (Figure 6b) demonstrated less decrease due to the better surface-protection of SWCNTs by wrapped CMC.

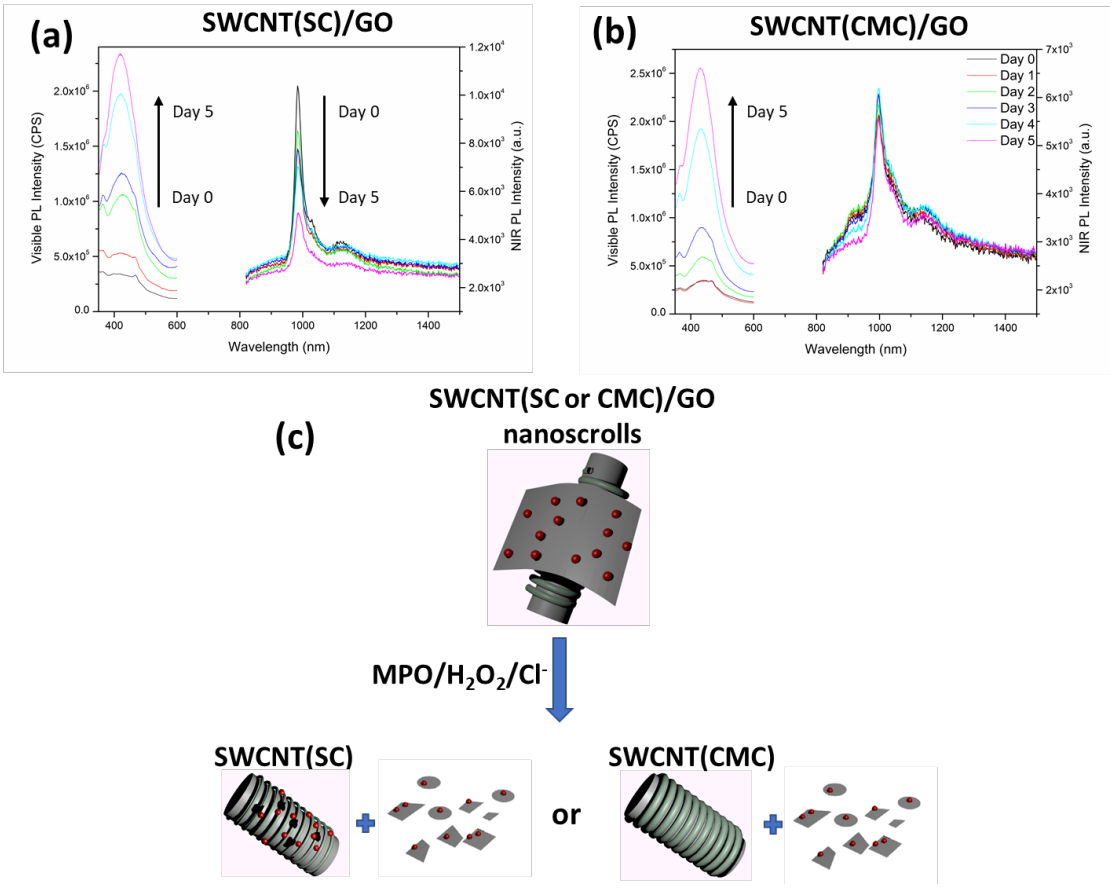

Figure 6. Photoluminescence spectra of MPO/H_2O_2/Cl^- degradation of SWCNT(SC)/GO (a) or SWCNT(CMC)/GO (b) nanoscrolls from Day 0 to Day 5. The visible and NIR PL spectra were taken under 325 nm and 566 nm excitation, respectively. (c) A schematic mechanism diagram illustrating the degradation of SWCNT/GO nanoscrolls (the oxygen-containing defect sites are shown in red).

Adopting a method similar to previously reported NIR ratiometric sensor systems,[68] we normalized the visible and NIR signal of both nanoscrolls systems. We plotted the relationship between the ratio of intensity (Ratio) over time based on the fitted linear correlation of both emission signals with time (t). Detailed definitions are as follows:

$$I_{GO}^{normalized}(t) = \frac{I_{GO}(t)}{I_{GO}(5)} \quad (1)$$

$$I_{SWCNT}^{normalized}(t) = \frac{I_{SWCNT}(t)}{I_{SWCNT}(0)} \quad (2)$$

$$Ratio(\mathrm{t}) = \frac{I_{GO}^{fitted}(t)}{I_{SWCNT}^{fitted}(t)} \quad (3)$$

Figure 7a and 7c show the normalized fluorescence intensity (Eq. 1 and 2) for both visible GO and NIR SWCNT signals as a function of time. The fitted linear regression lines exhibited a minimum R^2 value of 0.87 for the visible signals of both nanoscrolls. The NIR signals of SWCNT(SC)/GO sensor expressed a less rigorous correlation. The R^2 value of the NIR signal of SWCNT(CMC)/GO nanoscrolls was close to zero, which further confirmed that the NIR emission of CMC-wrapped remained invariant during the enzymatic oxidation. Figure 7b and 7d show the dependence of $Ratio(\mathrm{t})$ as a function of time for the MPO-catalyzed degradation. The result is the intensity of a pair of emission wavelengths that are representative of the oxidative stress in MPO/H_2O_2/Cl^- system independent of the absolute intensity. The $Ratio(\mathrm{t})$ values monotonically increased with time from Day 0 to Day 5. The quality of correlation proves that $Ratio(\mathrm{t})$ is a valuable method to monitor the oxidative stress caused by the MPO/H_2O_2/Cl^- system in both SWCNT(SC)/GO and SWCNT(CMC)/GO nanoscrolls. Looking forward, it would be interesting to visualize the degradation of nanoscrolls in terms of fluorescence microscopy. Applications can be made using fluorescence imaging technique to *in-situ* detect oxidative burst produced by MPO-secreting cells.

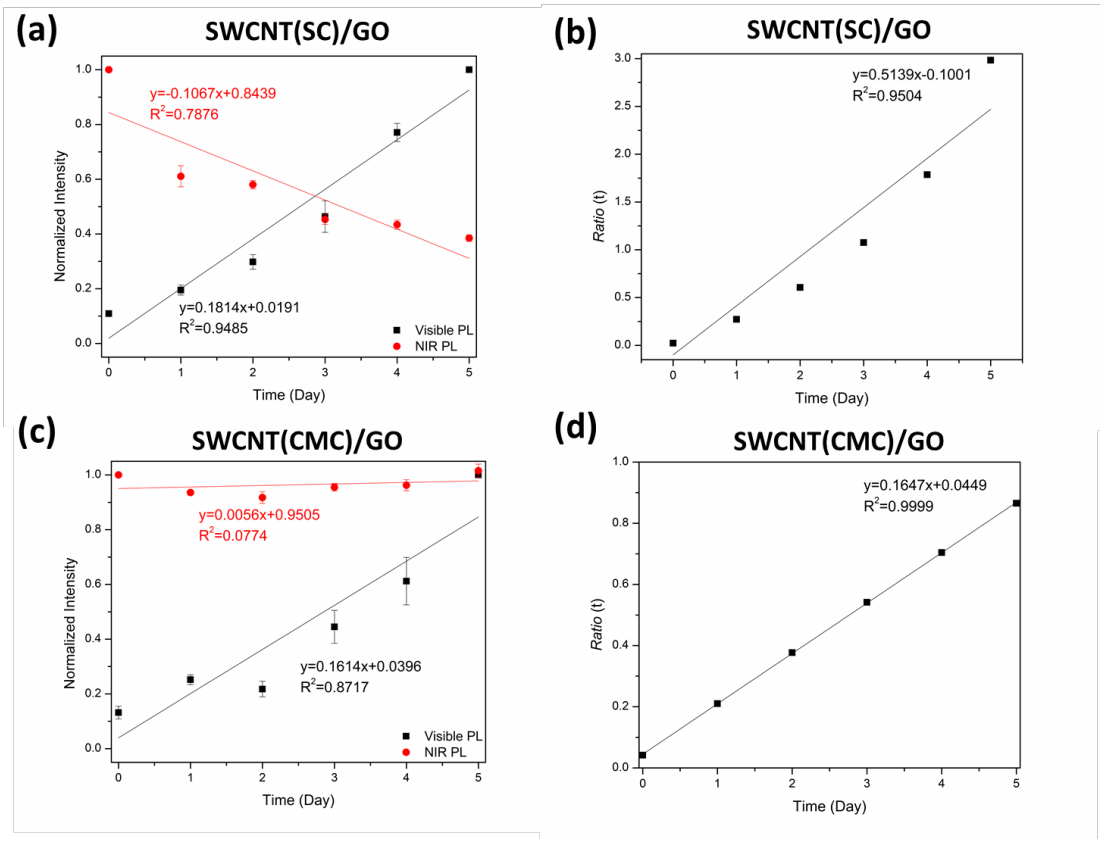

Figure 7. Changes in the SWCNT(SC)/GO (a, b) or SWCNT(CMC)/GO (c, d) nanoscrolls. The normalized photoluminescence intensity (a, c) and ratio of intensity (Ratio) (b, d) over 5-day MPO/H_2O_2/Cl^- degradation. The error bars represent standard deviations based on three replicate measurements.

Conclusion

In summary, we demonstrated, for the first time, the PL evolution during the MPO degradation of GO and SWCNT. Increased fluorescence emission at around 440 nm was observed with the progression of enzymatic oxidation of GO as a result of the formation of GQDs. The GO fluorescence was also used for monitoring MPO activity in neutrophil-like HL-60 cells. In contrast, the NIR E_{11} fluorescence of surfactant-coated SWCNT was either quenched (with SC) or remained almost unchanged (with CMC) during the 5-day degradation. The differences in surfactant coverage effected the ease of introducing defect sites on the sidewalls of SWCNTs. The two different PL systems were combined into a ratiometric

fluorescence sensor, which can be self-calibrated regardless of environmental noise. SWCNT/GO nanoscrolls have been demonstrated to be sensitive to the MPO-dependent oxidative inflammatory response. The increased PL of GO in the visible range acts as a turn-on sensor and the NIR PL signal from SWCNTs is used as the either turn-off or reference sensor. For both fluorescence ratiometers, the ratio of fluorescence intensity changed linearly with the progression of bio-oxidation process. This ratiometric optical sensing platform is applicable in complex environments such as strongly scattering media and biological tissues. In particular, as SWCNT(CMC)/GO system has the potential to be designed into a thin film sensor, our findings pave the way for the future development of the fluorescent sacrificial non-toxic solid state MPO activity indicators.

Supporting Information

UV-vis-NIR and PL spectra of SWCNT (SC), SWCNT(CMC) before and after dilution with H_2O, and SWCNT(CMC) or GO before and after 5-day degradation without MPO, H_2O_2, and Cl^-, respectively; EE maps of SWCNT (CMC) or GO before and after degradation; the normalized PL intensity of SWCNT(CMC) or GO over 5-day degradation; NIR or visible PL spectra of 5-day degradation without SWCNTs or GO, respectively; size distribution of GQDs; PL spectra of GO under different excitation wavelengths; comparison of water Raman peaks; Raman spectra and TEM images of GO before and after degradation without MPO, H_2O_2, and Cl^-, respectively; the subtracted PL spectra of GO after degradation; and AFM images and UV-vis-NIR spectra of SWCNT(SC) or SWCNT(CMC).

Acknowledgements

This material is based upon work supported by the National Science Foundation under grant no. 2003302. Raman characterization was completed through the assistance of a ONR (N000141410765) grant. We thank the Department of Biological Sciences and the Nanoscale Fabrication and Characterization Facility (NFCF) at the University of Pittsburgh for access to

the TEM, visible photoluminescence, DLS and zeta-potential instrumentation. We especially thank Dr. Bo Wegge Laursen for useful discussion about the fluorescence data. This work was supported, in part, by NIH HL114453, U19AI068021.

Author Information

Corresponding Author

Alexander Star — *Department of Chemistry and Department of Bioengineering, University of Pittsburgh, Pittsburgh, Pennsylvania 15260, United States; orcid.org/0000-0001-7863-5987; Email: astar@pitt.edu*

Authors

Xiaoyun He — *Department of Chemistry, University of Pittsburgh, Pittsburgh, Pennsylvania 15260, United States*

David L. White — *Department of Chemistry, University of Pittsburgh, Pittsburgh, Pennsylvania 15260, United States*

Alexandr A. Kapralov — *Department of Environmental and Occupational Health, University of Pittsburgh, Pittsburgh, Pennsylvania 15261, United States*

Valerian E. Kagan — *Department of Environmental and Occupational Health, University of Pittsburgh, Pittsburgh, Pennsylvania 15261, United States; orcid.org/0000-0002-7245-1885*

References

1. Witko-Sarsat, V.; Rieu, P.; Descamps-Latscha, B.; Lesavre, P.; Halbwachs-Mecarelli, L., Neutrophils: molecules, functions and pathophysiological aspects. *Lab. Invest.* **2000,** *80* (5), 617–653.

2. Hampton, M. B.; Kettle, A. J.; Winterbourn, C. C., Inside the neutrophil phagosome: oxidants, myeloperoxidase, and bacterial killing. *Blood* **1998,** *92* (9), 3007–3017.

3. Kagan, V. E.; Konduru, N. V.; Feng, W.; Allen, B. L.; Conroy, J.; Volkov, Y.; Vlasova, II; Belikova, N. A.; Yanamala, N.; Kapralov, A.; Tyurina, Y. Y.; Shi, J.; Kisin, E. R.; Murray, A. R.; Franks, J.; Stolz, D.; Gou, P.; Klein-Seetharaman, J.; Fadeel, B.; Star, A.; Shvedova, A. A., Carbon nanotubes degraded by neutrophil myeloperoxidase induce less pulmonary inflammation. *Nat. Nanotechnol.* **2010,** *5* (5), 354–359.

4. Vlasova, I. I.; Sokolov, A. V.; Chekanov, A. V.; Kostevich, V. A.; Vasilyev, V. B., Myeloperoxidase-induced biodegradation of single-walled carbon nanotubes is mediated by hypochlorite. *Bioorg. Khim.* **2011,** *37* (4), 510–521.

5. Vlasova, I. I.; Kapralov, A. A.; Michael, Z. P.; Burkert, S. C.; Shurin, M. R.; Star, A.; Shvedova, A. A.; Kagan, V. E., Enzymatic oxidative biodegradation of nanoparticles: Mechanisms, significance and applications. *Toxicol. Appl. Pharmacol.* **2016,** *299*, 58–69.

6. Bhattacharya, K.; Sacchetti, C.; El-Sayed, R.; Fornara, A.; Kotchey, G. P.; Gaugler, J. A.; Star, A.; Bottini, M.; Fadeel, B., Enzymatic 'stripping' and degradation of PEGylated carbon nanotubes. *Nanoscale* **2014,** *6* (24), 14686–14690.

7. Zhao, Y.; Burkert, S. C.; Tang, Y.; Sorescu, D. C.; Kapralov, A. A.; Shurin, G. V.; Shurin, M. R.; Kagan, V. E.; Star, A., Nano-gold corking and enzymatic uncorking of carbon nanotube cups. *J. Am. Chem. Soc.* **2015,** *137* (2), 675–684.

8. Burkert, S. C.; Shurin, G. V.; White, D. L.; He, X.; Kapralov, A. A.; Kagan, V. E.; Shurin, M. R.; Star, A., Targeting myeloid regulators by paclitaxel-loaded enzymatically degradable nanocups. *Nanoscale* **2018,** *10* (37), 17990–18000.

9. Kurapati, R.; Russier, J.; Squillaci, M. A.; Treossi, E.; Menard-Moyon, C.; Del Rio-Castillo, A. E.; Vazquez, E.; Samori, P.; Palermo, V.; Bianco, A., Dispersibility-Dependent Biodegradation of Graphene Oxide by Myeloperoxidase. *Small* **2015,** *11* (32), 3985–3994.

10. Mukherjee, S. P.; Gliga, A. R.; Lazzaretto, B.; Brandner, B.; Fielden, M.; Vogt, C.; Newman, L.; Rodrigues, A. F.; Shao, W.; Fournier, P. M.; Toprak, M. S.; Star, A.; Kostarelos,

K.; Bhattacharya, K.; Fadeel, B., Graphene oxide is degraded by neutrophils and the degradation products are non-genotoxic. *Nanoscale* **2018,** *10* (3), 1180–1188.

11. Chen, M.; Qin, X.; Zeng, G., Biodegradation of Carbon Nanotubes, Graphene, and Their Derivatives. *Trends in Biotechnol.* **2017,** *35* (9), 836–846.

12. Cao, L.; Meziani, M. J.; Sahu, S.; Sun, Y. P., Photoluminescence properties of graphene versus other carbon nanomaterials. *Acc. Chem. Res.* **2013,** *46* (1), 171–180.

13. Brozena, A. H.; Kim, M.; Powell, L. R.; Wang, Y., Controlling the optical properties of carbon nanotubes with organic colour-centre quantum defects. *Nat. Rev. Chem.* **2019,** *3* (6), 375–392.

14. Chiu, C. F.; Barth, B. A.; Kotchey, G. P.; Zhao, Y.; Gogick, K. A.; Saidi, W. A.; Petoud, S.; Star, A., Enzyme-catalyzed oxidation facilitates the return of fluorescence for single-walled carbon nanotubes. *J. Am. Chem. Soc.* **2013,** *135* (36), 13356–13364.

15. Chiu, C. F.; Dar, H. H.; Kapralov, A. A.; Robinson, R. A. S.; Kagan, V. E.; Star, A., Nanoemitters and innate immunity: the role of surfactants and bio-coronas in myeloperoxidase-catalyzed oxidation of pristine single-walled carbon nanotubes. *Nanoscale* **2017,** *9* (18), 5948–5956.

16. Huang, J.; Milton, A.; Arnold, R. D.; Huang, H.; Smith, F.; Panizzi, J. R.; Panizzi, P., Methods for measuring myeloperoxidase activity toward assessing inhibitor efficacy in living systems. *J. Leukocyte Biol.* **2016,** *99* (4), 541–548.

17. Querol, M.; Chen, J. W.; Bogdanov, Jr. A. A., A paramagnetic contrast agent with myeloperoxidase-sensing properties. *Org. Biomol. Chem.* **2006,** *4* (10), 1887–1895.

18. Rodriguez, E.; Nilges, M.; Weissleder, R.; Chen, J. W., Activatable magnetic resonance imaging agents for myeloperoxidase sensing: mechanism of activation, stability, and toxicity. *J. Am. Chem. Soc.* **2010,** *132* (1), 168–177.

19. Breckwoldt, M. O.; Chen, J. W.; Stangenberg, L.; Aikawa, E.; Rodriguez, E.; Qiu, S.; Moskowitz, M. A.; Weissleder, R., Tracking the inflammatory response in stroke in vivo by sensing the enzyme myeloperoxidase. *Proc. Natl. Acad. Sci. USA* **2008,** *105* (47), 18584–18589.

20. Hajnsek, M.; Schiffer, D.; Harrich, D.; Koller, D.; Verient, V.; Palen, J. v. d.; Heinzle, A.; Binder, B.; Sigl, E.; Sinner, F.; Guebitz, G. M., An electrochemical sensor for fast detection of wound infection based on myeloperoxidase activity. *Sens. Actuat. B: Chem.* **2015,** *209*, 265–274.

21. Borgmann, S., Electrochemical quantification of reactive oxygen and nitrogen: challenges and opportunities. *Anal. Bioanal. Chem.* **2009,** *394* (1), 95–105.

22. Calas-Blanchard, C.; Catanante, G.; Noguer, T., Electrochemical Sensor and Biosensor Strategies for ROS/RNS Detection in Biological Systems. *Electroanalysis* **2014,** *26* (6), 1277–1286.

23. Simões, E. F. C.; Leitão, J. M. M.; Da Silva, J., Carbon dots prepared from citric acid and urea as fluorescent probes for hypochlorite and peroxynitrite. *Microchim. Acta* **2016,** *183* (5), 1769–1777.

24. Yu, C.; Wu, Y.; Zeng, F.; Wu, S., A fluorescent ratiometric nanosensor for detecting NO in aqueous media and imaging exogenous and endogenous NO in live cells. *J. Mater. Chem. B* **2013,** *1* (33), 4152–4159.

25. Yin, B.; Deng, J.; Peng, X.; Long, Q.; Zhao, J.; Lu, Q.; Chen, Q.; Li, H.; Tang, H.; Zhang, Y.; Yao, S., Green synthesis of carbon dots with down-and up-conversion fluorescent properties for sensitive detection of hypochlorite with a dual-readout assay. *Analyst* **2013,** *138* (21), 6551–6557.

26. Wang, Q.; Tan, C.; Cai, W., A targetable fluorescent sensor for hypochlorite based on a luminescent europium complex loaded carbon nanotube. *Analyst* **2012,** *137* (8), 1872–1875.

27. Uusitalo, L. M.; Hempel, N., Recent advances in intracellular and *in vivo* ROS sensing: focus on nanoparticle and nanotube applications. *Int. J. Mol. Sci.* **2012,** *13* (9), 10660–10679.

28. Liu, X.; Han, Z.; Li, F.; Gao, L.; Liang, G.; Cui, H., Highly chemiluminescent graphene oxide hybrids bifunctionalized by N-(aminobutyl)-N-(ethylisoluminol)/horseradish peroxidase and sensitive sensing of hydrogen peroxide. *ACS Appl. Mater. Interfaces* **2015,** *7* (33), 18283–18291.

29. Zan, X.; Fang, Z.; Wu, J.; Xiao, F.; Huo, F.; Duan, H., Freestanding graphene paper decorated with 2D-assembly of Au@Pt nanoparticles as flexible biosensors to monitor live cell secretion of nitric oxide. *Biosens. Bioelectron.* **2013,** *49*, 71–78.

30. Yeh, T. Y.; Wang, C. I.; Chang, H. T., Photoluminescent C-dots@ RGO for sensitive detection of hydrogen peroxide and glucose. *Talanta* **2013,** *115*, 718–723.

31. Doussineau, T.; Schulz, A.; Lapresta-Fernandez, A.; Moro, A.; Korsten, S.; Trupp, S.; Mohr, G. J., On the design of fluorescent ratiometric nanosensors. *Chem. Eur. J.* **2010,** *16* (34), 10290–10299.

32. Yoon, S. M.; Kim, S. J.; Shin, H. J.; Benayad, A.; Choi, S. J.; Kim, K. K.; Kim, S. M.; Park, Y. J.; Kim, G.; Choi, J. Y.; Lee, Y. H., Selective oxidation on metallic carbon nanotubes by halogen oxoanions. *J. Am. Chem. Soc.* **2008,** *130* (8), 2610–2616.

33. Wu, C. H., Studies of the equilibrium and thermodynamics of the adsorption of Cu(2+) onto as-produced and modified carbon nanotubes. *J. Colloid Interface Sci.* **2007,** *311* (2), 338–346.

34. Kotchey, G. P.; Gaugler, J. A.; Kapralov, A. A.; Kagan, V. E.; Star, A., Effect of antioxidants on enzyme-catalysed biodegradation of carbon nanotubes. *J. Mater. Chem. B* **2013,** *1* (3), 302–309.

35. Kotchey, G. P.; Hasan, S. A.; Kapralov, A. A.; Ha, S. H.; Kim, K.; Shvedova, A. A.; Kagan, V. E.; Star, A., A natural vanishing act: the enzyme-catalyzed degradation of carbon nanomaterials. *Acc. Chem. Res.* **2012,** *45* (10), 1770–1781.

36. Bai, H.; Jiang, W.; Kotchey, G. P.; Saidi, W. A.; Bythell, B. J.; Jarvis, J. M.; Marshall, A. G.; Robinson, R. A.; Star, A., Insight into the Mechanism of Graphene Oxide Degradation via the Photo-Fenton Reaction. *J. Phys. Chem. C* **2014,** *118* (19), 10519–10529.

37. Sannino, A.; Demitri, C.; Madaghiele, M., Biodegradable Cellulose-based Hydrogels: Design and Applications. *Materials* **2009,** *2* (2), 353–373.

38. Schurz, J., A bright future for cellulose. *Prog. Polym. Sci.* **1999,** *24* (4), 481–483.

39. Wang, B.; Du, X.; Wang, M.; Gong, W.; Anzai, J., A Facile Preparation of H_2O_2 Sensors Using Layer-by-Layer Deposited Thin Films Composed of Poly (ethyleneimine) and Carboxymethyl Cellulose as Matrices for Immobilizing Hemin. *Electroanalysis* **2008,** *20* (9), 1028–1031.

40. Shibraen, M. H. A.; Yagoub, H.; Wang, Z.; Yang, S., Influence of Operational Parameters on Layer-by-layer Assembled Cellulose Derivatives Thin Film. *2nd Annual International Conference on Advanced Material Engineering (AME 2016)*, Atlantis Press: **2016**.

41. Bachilo, S. M.; Strano, M. S.; Kittrell, C.; Hauge, R. H.; Smalley, R. E.; Weisman, R. B., Structure-Assigned Optical Spectra of Single-Walled Carbon Nanotubes. *Science* **2002,** *298* (5602), 2361–2366.

42. Hilmer, A. J.; McNicholas, T. P.; Lin, S.; Zhang, J.; Wang, Q. H.; Mendenhall, J. D.; Song, C.; Heller, D. A.; Barone, P. W.; Blankschtein, D.; Strano, M. S., Role of adsorbed surfactant in the reaction of aryl diazonium salts with single-walled carbon nanotubes. *Langmuir* **2012,** *28* (2), 1309–1321.

43. Kotchey, G. P.; Allen, B. L.; Vedala, H.; Yanamala, N.; Kapralov, A. A.; Tyurina, Y. Y.; Klein-Seetharaman, J.; Kagan, V. E.; Star, A., The enzymatic oxidation of graphene oxide. *ACS Nano* **2011,** *5* (3), 2098–2108.

44. Zhou, X.; Zhang, Y.; Wang, C.; Wu, X.; Yang, Y.; Zheng, B.; Wu, H.; Guo, S.; Zhang, J., Photo-Fenton reaction of graphene oxide: a new strategy to prepare graphene quantum dots for DNA cleavage. *ACS Nano* **2012,** *6* (8), 6592–6599.

45. Heinecke, J. W.; Li, W.; Daehnke, H. L., 3rd; Goldstein, J. A., Dityrosine, a specific marker of oxidation, is synthesized by the myeloperoxidase-hydrogen peroxide system of human neutrophils and macrophages. *J. Biol. Chem.* **1993,** *268* (6), 4069–4077.

46. Harms, G. S.; Pauls, S. W.; Hedstrom, J. F.; Johnson, C. K., Fluorescence and Rotational Dynamics of Dityrosine. *J. Fluoresc.* **1997,** *7* (4), 283–292.

47. Martin, S. F.; Wood, A. D.; McRobbie, M. M.; Mazilu, M.; McDonald, M. P.; Samuel, I. D. W.; Herrington, C. S., Fluorescence spectroscopy of an in vitro model of human cervical precancer identifies neoplastic phenotype. *Int. J. Cancer* **2007,** *120* (9), 1964–1970.

48. Ansari, M. A.; Erfanzadeh, M.; Mohajerani, E., Mechanisms of Laser-Tissue Interaction: II. Tissue Thermal Properties. *J. Lasers Med. Sci.* **2013,** *4* (3), 99–106.

49. Orecchioni, M.; Bedognetti, D.; Sgarrella, F.; Marincola, F. M.; Bianco, A.; Delogu, L. G., Impact of carbon nanotubes and graphene on immune cells. *J. Transl. Med.* **2014,** *12* (1), 138.

50. Gallagher, R.; Collins, S.; Trujillo, J.; McCredie, K.; Ahearn, M.; Tsai, S.; Metzgar, R.; Aulakh, G.; Ting, R.; Ruscetti, F.; Gallo, R., Characterization of the continuous, differentiating myeloid cell line (HL-60) from a patient with acute promyelocytic leukemia. *Blood* **1979,** *54* (3), 713–733.

51. Ye, R.; Xiang, C.; Lin, J.; Peng, Z.; Huang, K.; Yan, Z.; Cook, N. P.; Samuel, E. L. G.; Hwang, C.-C.; Ruan, G.; Ceriotti, G.; Raji, A.-R. O.; Martí, A. A.; Tour, J. M., Coal as an abundant source of graphene quantum dots. *Nat. Commun.* **2013,** *4* (1), 2943.

52. Liu, F.; Jang, M.-H.; Ha, H. D.; Kim, J.-H.; Cho, Y.-H.; Seo, T. S., Facile Synthetic Method for Pristine Graphene Quantum Dots and Graphene Oxide Quantum Dots: Origin of Blue and Green Luminescence. *Adv. Mater.* **2013,** *25* (27), 3657–3662.

53. Wang, S.; Cole, I. S.; Zhao, D.; Li, Q., The dual roles of functional groups in the photoluminescence of graphene quantum dots. *Nanoscale* **2016,** *8* (14), 7449–7458.

54. Kungl, A. J.; Landl, G.; Visser, A. J. W. G.; Breitenbach, M.; Kauffmann, H. F., l-Dityrosine: A time-resolved fluorescence investigation. *J. Fluoresc.* **1992,** *2* (1), 63–73.

55. Chang, N.; Lu, Y.; Mao, J.; Yang, J.; Li, M.; Zhang, S.; Liu, Y., Ratiometric fluorescence sensor arrays based on quantum dots for detection of proteins. *Analyst* **2016,** *141* (6), 2046–2052.

56. Huang, C.; Jia, T.; Tang, M.; Yin, Q.; Zhu, W.; Zhang, C.; Yang, Y.; Jia, N.; Xu, Y.; Qian, X., Selective and Ratiometric Fluorescent Trapping and Quantification of Protein Vicinal Dithiols and in Situ Dynamic Tracing in Living Cells. *J. Am. Chem. Soc.* **2014,** *136* (40), 14237–14244.

57. Han, J.; Zhang, C.; Liu, F.; Liu, B.; Han, M.; Zou, W.; Yang, L.; Zhang, Z., Upconversion nanoparticles for ratiometric fluorescence detection of nitrite. *Analyst* **2014,** *139* (12), 3032–3038.

58. Dong, X.; Xing, G.; Chan-Park, M. B.; Shi, W.; Xiao, N.; Wang, J.; Yan, Q.; Sum, T. C.; Huang, W.; Chen, P., The formation of a carbon nanotube–graphene oxide core–shell structure and its possible applications. *Carbon* **2011,** *49* (15), 5071–5078.

59. Li, Y.; Yang, T.; Yu, T.; Zheng, L.; Liao, K., Synergistic effect of hybrid carbon nantube–graphene oxide as a nanofiller in enhancing the mechanical properties of PVA composites. *J. Mater. Chem.* **2011,** *21* (29), 10844–10851.

60. Wimalasiri, Y.; Zou, L., Carbon nanotube/graphene composite for enhanced capacitive deionization performance. *Carbon* **2013,** *59*, 464–471.

61. Zhang, C.; Ren, L.; Wang, X.; Liu, T., Graphene Oxide-Assisted Dispersion of Pristine Multiwalled Carbon Nanotubes in Aqueous Media. *J. Phys. Chem. C* **2010,** *114* (26), 11435–11440.

62. White, B.; Banerjee, S.; O'Brien, S.; Turro, N. J.; Herman, I. P., Zeta-Potential Measurements of Surfactant-Wrapped Individual Single-Walled Carbon Nanotubes. *J. Phys. Chem. C* **2007,** *111* (37), 13684–13690.

63. Kim, Y.-K.; Min, D.-H., Preparation of scrolled graphene oxides with multi-walled carbon nanotube templates. *Carbon* **2010,** *48* (15), 4283–4288.

64. Ishibashi, A.; Nakashima, N. Strong chemical structure dependence for individual dissolution of single-walled carbon nanotubes in aqueous micelles of biosurfactants. *Bull. Chem. Soc. Jpn.* **2006,** *79*(2), 357–359.

65. Riou, I.; Bertoncini, P.; Bizot, H.; Mevellec, J. Y.; Buléon, A.; & Chauvet, O. Carboxymethylcellulose/single walled carbon nanotube complexes. *J. Nanosci. Nanotechno.* **2009**, *9*(10), 6176–6180.

66. Salavagione, H. J.; Díez-Pascual, A. M.; Lázaro, E.; Vera, S.; Gómez-Fatou, M. A., Chemical sensors based on polymer composites with carbon nanotubes and graphene: the role of the polymer. *J. Mater. Chem. A* **2014,** *2* (35), 14289–14328.

67. Choi, J. H.; Strano, M. S., Solvatochromism in single-walled carbon nanotubes. *Appl. Phys. Lett.* **2007,** *90* (22), 223114.

68. Giraldo, J. P.; Landry, M. P.; Kwak, S. Y.; Jain, R. M.; Wong, M. H.; Iverson, N. M.; Ben-Naim, M.; Strano, M. S., A Ratiometric Sensor Using Single Chirality Near-Infrared Fluorescent Carbon Nanotubes: Application to In Vivo Monitoring. *Small* **2015,** *11* (32), 3973–3984.

TOC